# Investigation of radiative bow-shocks in magnetically accelerated plasma flows

S. C. Bott-Suzuki, L. S. Caballero Bendixsen, S. W. Cordaro, I. C. Blesener, C. L. Hoyt, A. D. Cahill, B. R. Kusse, D. A. Hammer, P. A. Gourdain, C. E. Seyler, J. B. Greenly, J. P. Chittenden, N. Niasse, S. V. Lebedev, and D. J. Ampleford

Citation: Physics of Plasmas **22**, 052710 (2015); doi: 10.1063/1.4921735
View online: http://dx.doi.org/10.1063/1.4921735
View Table of Contents: http://scitation.aip.org/content/aip/journal/pop/22/5?ver=pdfcov
Published by the AIP Publishing



# Investigation of radiative bow-shocks in magnetically accelerated plasma flows

S. C. Bott-Suzuki,[1,a)] L. S. Caballero Bendixsen,[1] S. W. Cordaro,[1] I. C. Blesener,[2] C. L. Hoyt,[2] A. D. Cahill,[2] B. R. Kusse,[2] D. A. Hammer,[2] P. A. Gourdain,[2] C. E. Seyler,[2] J. B. Greenly,[2] J. P. Chittenden,[3] N. Niasse,[3] S. V. Lebedev,[3] and D. J. Ampleford[4]
[1]*University of California San Diego, La Jolla, California 92093, USA*
[2]*Cornell University, Ithaca, New York 14850, USA*
[3]*Imperial College London, South Kensington, London SW7 2BW, United Kingdom*
[4]*Sandia National Laboratories, Albuquerque, New Mexico 87185, USA*

(Received 19 February 2015; accepted 13 May 2015; published online 29 May 2015)

We present a study of the formation of bow shocks in radiatively cooled plasma flows. This work uses an inverse wire array to provide a quasi-uniform, large scale hydrodynamic flow accelerated by Lorentz forces to supersonic velocities. This flow impacts a stationary object placed in its path, forming a well-defined Mach cone. Interferogram data are used to determine a Mach number of ~6, which may increase with radial position suggesting a strongly cooling flow. Self-emission imaging shows the formation of a thin (<60 $\mu$m) strongly emitting shock region, where $T_e \sim 40$–50 eV, and rapid cooling behind the shock. Emission is observed upstream of the shock position which appears consistent with a radiation driven phenomenon. Data are compared to 2-dimensional simulations using the Gorgon MHD code, which show good agreement with the experiments. The simulations are also used to investigate the effect of magnetic field in the target, demonstrating that the bow-shocks have a high plasma $\beta$, and the influence of B-field at the shock is small. This consistent with experimental measurement with micro bdot probes. © *2015 AIP Publishing LLC*. [http://dx.doi.org/10.1063/1.4921735]

## I. INTRODUCTION

Radiation loss in shock systems is common to several areas of scientific intrigue, including in many astrophysical and inertial fusion systems. A particularly dramatic example is that of Young Stellar Object (YSO) jets (e.g., Refs. 1 and 2) which form complex bow shock structures as the jet interacts with the interstellar medium. In adiabatic systems, the increase in density of the flow as it traverses the discontinuity which defines the shock is determined by the ratio of specific heats, $\gamma$. For a monotonic gas this is equal to 5/3. If the flow arriving at the shock, the upstream flow, has known quantities for density, temperature and pressure, the values of these after the shock (downstream) can be analytically calculated from the Rankine-Hugoniot equations.[3–6] These are derived from the conservation of momentum and energy across the shock and for a strong shock the density increase is limited to values of $(\gamma+1)/(\gamma-1)=4$. When radiation is emitted during the formation of a shock this behaves as a loss mechanism in the energy equation and allows greater density compression across the shock front. The effective $\gamma$ is 4/3 or lower, giving a compression of 7 if radiation is trapped local to the shock, and greater than this if the radiation can escape. This loss of energy during compression also affects the temperature increase at the shock and the rate at which the post shock flow cools behind it.

For a small obstruction in a supersonic flow, the angle of the bow shock formed around it, the Mach cone, is directly determined by the upstream (pre-shock) sonic Mach number, and so be used to examine the inflow conditions. Whilst shocks in which radiation losses play a significant role are common is astrophysics, they can be difficult to generate and characterize in the laboratory. Such shocks have been successfully demonstrated by several authors in various geometries including spherical blast-waves, and laser-driven planar shock tube and cluster explosion experiments.[7–14] The continued examination of shock formation in the appropriate regimes is vital to developing a thorough theoretical basis for their analysis in astrophysical and related systems. In this work, we demonstrate quasi-2D, stationary (in the lab frame) bow shocks which allow examination of the shock details and the effect of the radiative energy loss associated with both the upstream flow and compression in the shock itself. Observations of bow shocks in wire array systems were first reported by Ampleford *et al.*[15] using gated self-emission imaging of nested wire arrays. Preliminary work on the set-up used in the study reported here was presented by Peebles *et al.*[16] using laser imaging interferometry. Here, we present the first detailed measurements using both diagnostics in tandem to demonstrate the formation of a Mach cone, along with high resolution 2-dimensional magneto-hydrodynamic simulations.

## II. EXPERIMENTAL ARRANGEMENT

The experimental setup uses an inverse wire array[17] to generate a supersonic, hydrodynamic plasma flow, which then interacts with a small obstruction generating a bow shock. In pulsed-power driven exploding wire experiments, the acceleration of plasma is achieved through the Lorentz

a)Electronic mail: sbottsuzuki@ucsd.edu

 

($\mathbf{j} \times \mathbf{B}$) force, where $\mathbf{j}$ is the current density in the load wires and $\mathbf{B}$ is the "global" magnetic field around the entire array. Typical drive currents in a single metallic wire can be of order 20–100 kA, giving accelerating B-fields of order of a few Tesla for typical wire array diameters, and current densities $>10^{14}$ A/m$^2$. The acceleration of plasma ablated from the wires occurs over very short ranges and the flow may propagate >10 mm. Temperatures are ~15 eV, and flow velocities are ~100 km s$^{-1}$ which can be several times the local sound speed.

The rate of mass ablation from the wires in a cylindrical wire array, *dm/dt*, can be well approximated analytically by balancing the average momentum of the flow with the accelerating magnetic pressure.[18] For an inverse wire array, algebraic rearrangement is required to account for the radially outward flow, and converting mass density into areal electron density allows direct comparison to interferogram unfolds where no inference of symmetry in the flow is required[17]

$$n_e L(r,t) = \frac{\mu_0 Z}{4\pi V_{abl}^2 R_0 N_w A m_p}\left[I\left(t - \frac{r - R_0}{V_{abl}}\right)\right]^2. \quad (1)$$

Here, Z is the ionization state, $m_p$ is the proton mass, r is the radial position from the center of the array being analyzed, $R_0$ is the radius of the array, and A is the atomic weight of the material. The parameter $V_{abl}$ is a scaling parameter based on the fluid flow velocity. The most detailed direct measurements of the flow velocity are those of Harvey-Thompson *et al.*,[19–21] who find velocities of ~100 km/s for tungsten wire arrays. Here, we use this value and assume this is fixed throughout the experiment, which is in general agreement with MHD simulations presented below. From Ref. 18, the mass density at a given radial position can be determined as a function of time using a fixed value for *r* in

$$\rho(r,t) = \frac{\mu_0}{8\pi^2 r R_0 V_{abl}^2}\left[I\left(\frac{R_0 - r}{V_{abl}}\right)\right]^2. \quad (2)$$

For this work, we require that the plasma flows produced by the inverse wire array are collisional on the scale length of the interaction at the obstruction. The experiments were carried out on the XP generator at Cornell University[22] in a "long-pulse" mode, which provides a peak current $I_{max} = 260$ kA, which peaks at $\tau = 145$ ns with the form $I(t) = I_{max}\sin^2(\pi t/2\tau)$. A schematic of the set-up, along with a photograph is given in Figure 1. The targets to be used are 25 $\mu$m Al wires mounted on electrically isolated platforms remote from the load, formed as long loops running through the 2-dimensional plane of the plasma flow. The interaction of the flow with the target is limited to a ~1 mm region at the apex of the loop where the target wires runs perpendicular to the flow direction. As shown below, the flow is highly supersonic, and therefore expansion in the azimuthal direction is very small over the scale lengths of interest.

Given an array diameter of 10 mm and using two tungsten wires in the inverse array, the electron density and ion density (using an assumed $T_e = 15$ eV a mean ionization state Z of 10) at an obstruction place 5 mm radially outwards from the wire can be calculated though Eq. (2). This is plotted in Figure 2. For these plots, the plasma flow thickness is assumed to be 1 mm to allow a conversion to volumetric densities.

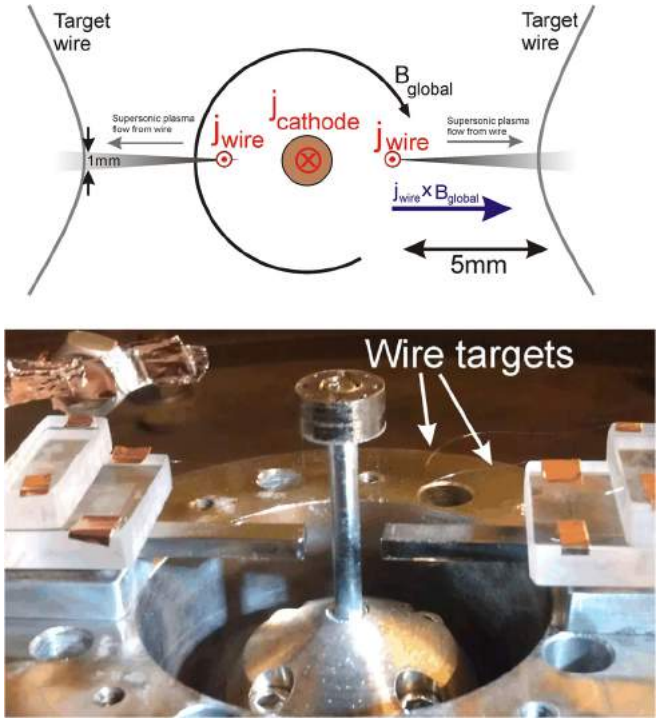


FIG. 1. Schematic (top view) and photograph (side view) of the inverse wire array set up fielded on the XP generator at Cornell University.

The flight time of the plasma flow from the wire to the obstruction is ~35 ns, and after 80 ns the ion mean free path (e.g., Ref. 23) here is <100 $\mu$m, and after 125 ns is <10 $\mu$m. It can therefore be safely assumed that the flow is entirely hydrodynamic if the shock region spatial scale is of order a few 10 s of microns or greater in the ~100 ns window around peak current. It should be noted that the ion-ion mean free path is sensitive to several parameters, notably the ionization state; $\lambda_{ion}$ scale as $Z^{-4}$ (e.g., Ref. 24). In this work, the ionization state is not established independently, and is estimated from a Thomas-Fermi approach (e.g., Ref. 25). We expect this to be a good approximation, and the hydrodynamic nature of the interaction is confirmed by experimental measurements of the shock presented below, along with the discussion of the role of magnetic field. One further point regarding the ablated plasma flow is that this is non-uniform in the axial direction. The density contrast across the flare structure has been measured in various experiments to be of order 2 or less,[17,26] and so this variation has a negligible effect on the collisionality at the obstruction.

The primary diagnostics are 2-frame laser interferometer using a 150 ps, 532 nm Nd:YAG laser and extreme ultraviolet (XUV) self-emission pinhole imaging combined with a micro-channel plate (MCP) to enable a temporal resolution of 10 ns. Images are obtained along the same line-of-sight using a new diagnostic set-up recently developed.[27] Interferometry images are analyzed using the IDEA

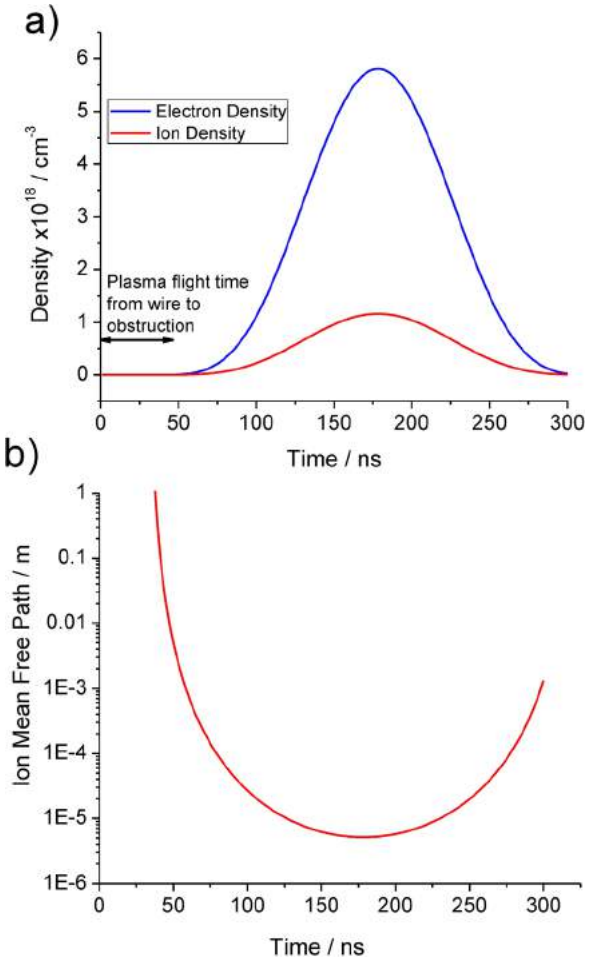


FIG. 2. Plots for a 2 wire inverse tungsten wire array showing (a) electron and ion density (assuming z = 10) and (b) mean free ion paths at an obstruction 5 mm radially outwards from the wire as a function of time.

software.[28,29] IDEA uses a 2-dimensional spatial fast Fourier transform (FFT) to isolate the carrier frequency and compare the experimental image with a background (no plasma) image. The phase shift $\Delta\phi$ induced by the plasma is proportional to the laser frequency, the critical density in the plasma,[30] and the plasma density. The fringe shift measured in the experiment can then be plotted as a function of space and converted to areal (i.e., integrated along the line of sight of the diagnostic) electron density through Eq. (1). The accuracy to which the fringes can be resolved is typically ~1/4 fringe shift, ($n_{e,areal} \sim 1 \times 10^{17}$ cm$^{-2}$), and the spatial resolution of the images is ~50 $\mu$m.

The self-emission diagnostic used a typical pinhole camera set up, with four pinholes imaging onto four independently gated frames of a microchannel plate (MCP). The spatial and energy resolution of the image is determined by the pinhole diameter and magnification of the image. For this work typically 2 different pinhole sizes were used, 200 $\mu$m and 50 $\mu$m, which for a magnification of ~0.6 gives a spatial resolution of ~500 $\mu$m for energies > 10 eV for the larger pinholes, and ~100 $\mu$m for energies > 160 eV for the smaller. Comparison of the images using the two different pinholes at similar times in the experiment therefore allows estimation of the plasma temperature in various regions.

## III. RESULTS

A series of experiments was carried out, and data are presented and analyzed in this section. Figure 3 shows a sequence of interferograms taken during the formation of the shock (note that these are taken from different experiments, and so the exact locations of the source and target wires vary slightly). Initially, the interferogram frame shows no electron density at the target, and the first clear fringe shift is observed at ~40 ns, in general agreement with the estimations above. The density increases rapidly after this due to both the increasing absolute upstream density and the rapid reduction of the collisional mean free path. The density gradient in front of the target continues to increase, and is soon beyond the measurement range of the interferometer. Whilst the straight through position of the shock is therefore not quantifiable directly, the "wings" of the bow shock can be readily analyzed. Figure 4 shows pre-shot and shot interferometer images, and the small area around the shock is analyzed in Figure 5. The resultant areal electron density map is given below in the same figure. Here, a small section of the upstream flow is visible, along with regions close to and downstream of the shock. A lineout can be taken perpendicular to the flow direction, which shows areal densities of ~$6 \times 10^{17}$ cm$^{-2}$ along with the typical ablation flares which show density variation of ~10% of this value.

As is clear from the raw interferogram, it is not possible to examine the peak compression at the shock using this diagnostic. The regions around the shock, however, clearly

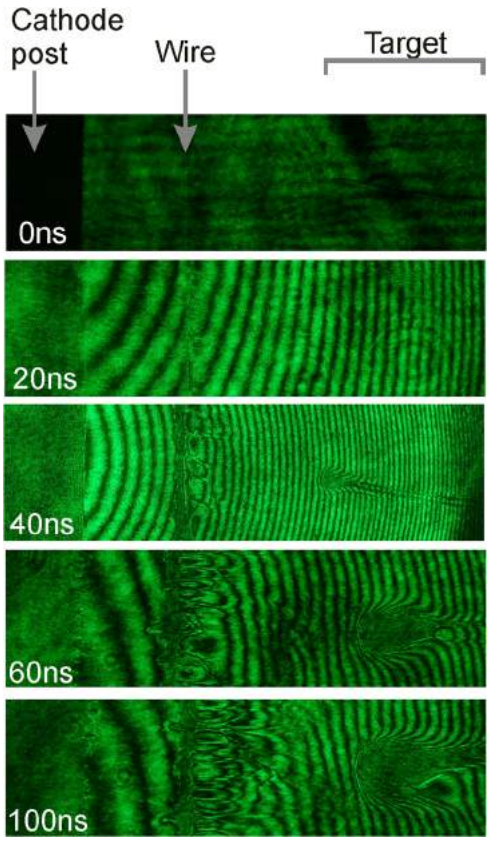


FIG. 3. Interferogram time sequence (different shots) showing evolution of the plasma density at a static target placed in the flow (Note target and wire placements are slightly different for different shots).

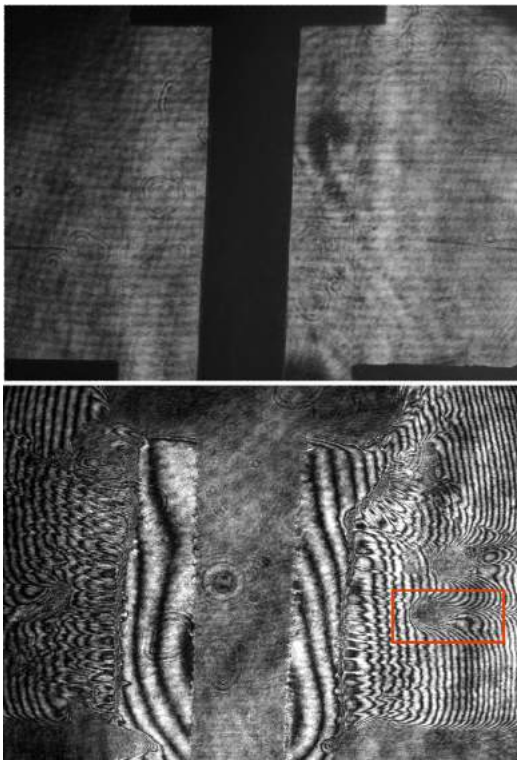

FIG. 4. Pre-shot shadow image showing position of ablating wires and targets, and interferogram taken at 115 ns into the current drive. The region in the box is analyzed in Figure 5.

delineate a Mach cone, and the angle of this relative to the flow direction can be measured. Since this angle is related to the upstream Mach number through $\sin(\alpha) = 1/M$ we can characterize the upstream flow as a function of the position of the target and time. This is shown in Figure 6. Note that we only analyze data in which the targets are perpendicular to flow (as determined from pre-shot images under vacuum). For example, the upper shock in Figure 4 was not included in calculation of the upstream Mach number since the pre-shot image clearly shows that the target is not perpendicular to the diagnostic view, which would likely infer a wider shock angle (and hence lower Mach number) than would otherwise be measured.

Figure 6 shows measurements taken for shocks at similar times over a small range of radial position from the load wire. The error on the measurement is driven by the sensitivity to the angle measurement at high Mach number (small half angle). We see that the flow is strongly supersonic, and may slowly increase with increasing radial position. This would be consistent with a plasma flow that cools through radiation loss as it approaches the target. For an approximately fixed velocity this results in a reduced $T_e$ and sound speed, and hence increased Mach number. Whilst the trend here is difficult to discern clearly, this is the first direct measurement of the sonic Mach number in inverse wire array ablated flows. Here, we find $M = 6 +/- 2.45$ which is in the range of $M \sim 4$–12 quoted by Ampleford *et al.*[15] for nested wire array experiments at similar flow densities and in line with the simulations below.

The bow-shocks have also been examined using time-gated self-emission, and the two frames in Figure 7 are taken

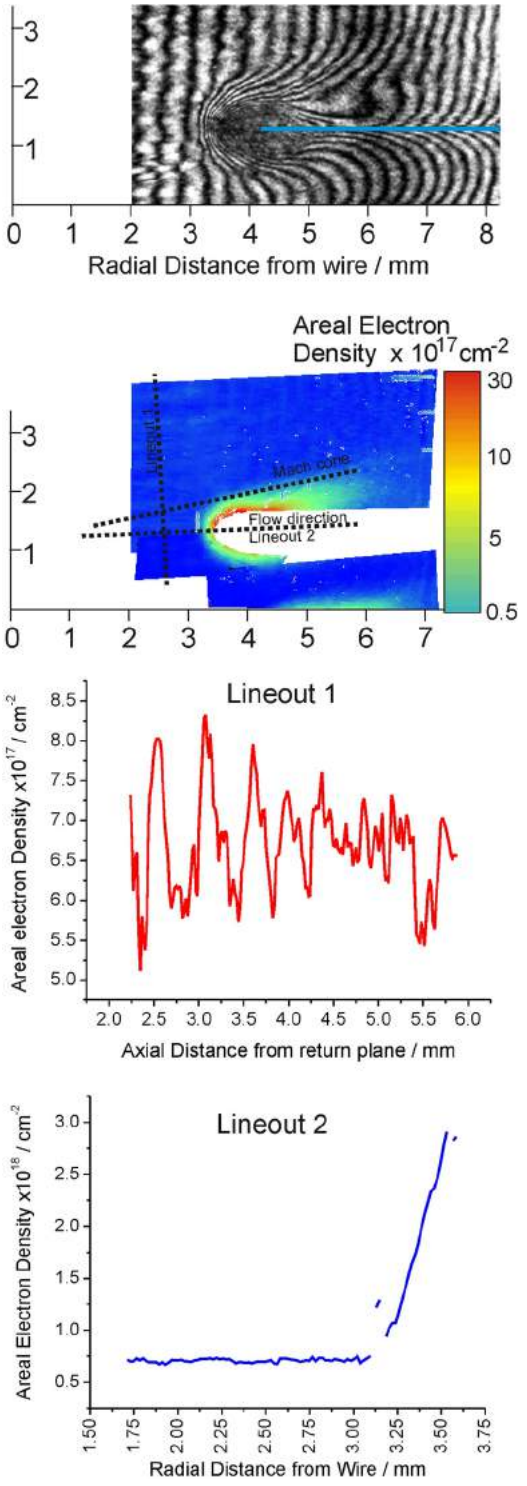


FIG. 5. Analysis of shock for a W array at 115 ns: (a) scaled high magnification raw interferogram, (b) areal electron density from interferogram unfold, and plots of areal electron density in (c) axial direction to demonstrate low density variation and d) parallel to flow direction leading up to bow shock.

at similar times in the same experiment using different sized pinholes as described above. The left image ($h\nu > 10$ eV) shows much of the detail associated with the exploding wire and accelerated plasma flow, along with the interaction of the flow with each obstruction. The emission increases significantly at the shock region and again a clear Mach cone is formed about the obstruction. Following the emission

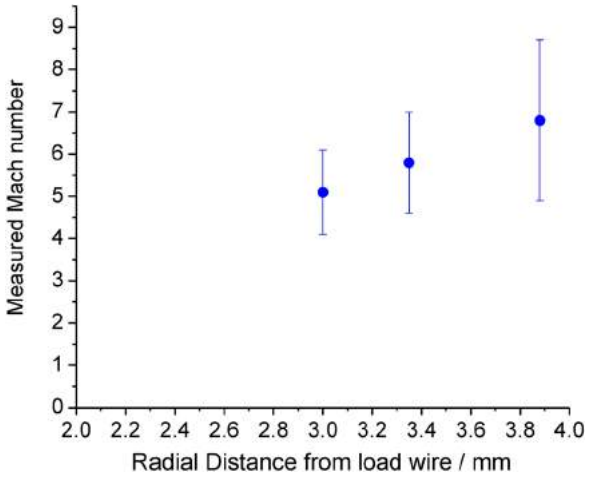


FIG. 6. Plot of the variation of the upstream Mach number as a function of radius as determined by analysis of the bow shock Mach cone angle.

increase at the shock, the emission is reduced indicating strong cooling across the shock region, and a relatively small shock width is observed. In the higher photon energy image ($h\nu > 160$ eV, right image in Fig. 7), only the very apex of the shock region is visible, and this only weakly. From the comparison of the two images, we can deduce that the upstream plasma flow is relatively cool, in line with ~15 eV taken above. Approximating the emission spectral output to a blackbody for tungsten and taking the photon energy imaged by the pinhole arrangement as the peak in that spectrum, we can estimate that the plasma temperature peaks at ~40–50 eV at the shock. This is likely a lower estimate but is in general agreement with the collision of similar plasma streams in cylindrical wire arrays.[31–33]

Self-emission images were also taken with a higher magnification arrangement, which gave a spatial resolution of ~80 $\mu$m for photon energies > 80 eV. An example is given in Figure 8. The shock emission is a very well defined region of ~60 $\mu$m. This is comparable to the spatial resolution of the diagnostic, so this is likely an upper limit for this width. Behind the shock, the emission drops very rapidly, again indicating very strong cooling across the shock. It is also interesting to note that there appears to be significant emission ahead of the shock position, extending ~0.5 mm into the upstream flow. The form of the emission closely follows the Mach cone and appears more pronounced at the

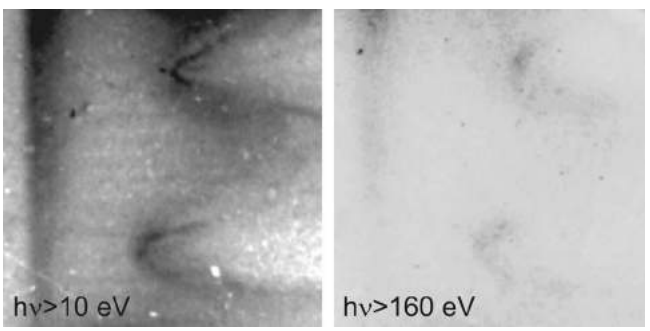


FIG. 7. Gated self-emission (10 ns) pinhole images taken at the same time (125 ns) on the same shot, but with differing diffraction-limited photon energy ranges.

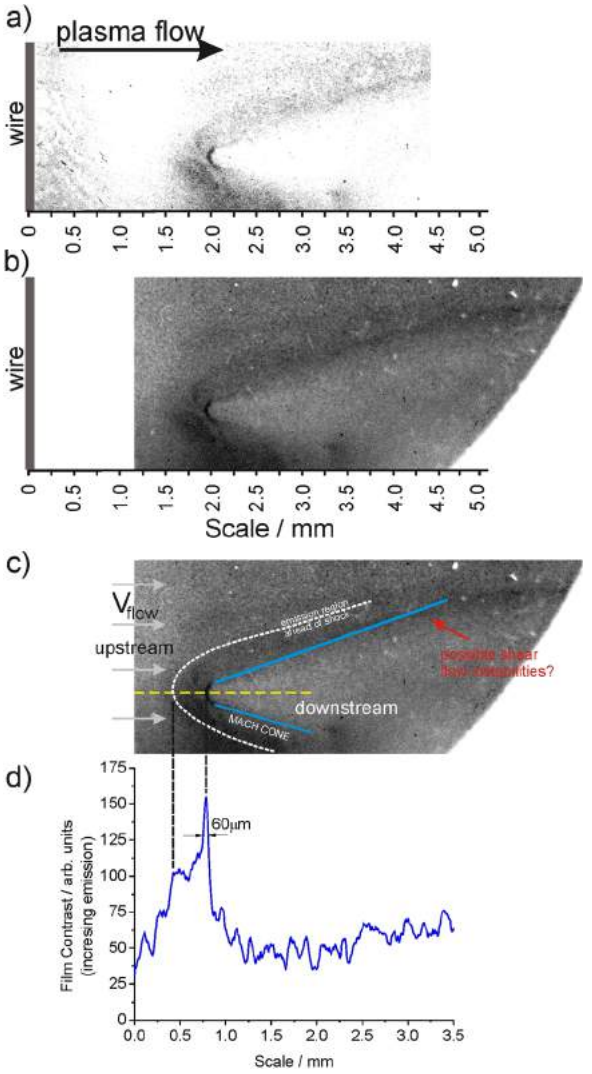


FIG. 8. A typical gated self-emission image ($h\nu > 80$ eV) of bow-shock formation in a tungsten plasma flow at 125 ns: (a) high contrast image, (b) typical image from detector film, (c)same image in a and b with annotations, and (d) lineout through dashed yellow line in (c).

apex. Several mechanisms could cause such features and careful analysis is required to determine the likely cause. These are discussed in Sec. V.

One possible influence on the shock formation is the presence of magnetic field advected by the plasma flow from the wires. Typically, the magnetic Reynolds number in wire array experiments is estimated to be ~1, suggesting that little B-field is advected downstream (e.g., Ref. 18). Here, we use micro b-dot probes[34] to measure directly the magnetic flux at 2 radial positions. In these experiments, we removed the bow-shock targets, and examined the ablating wire array flow only. The micro-bdots were placed at 4 mm from the load wire, the location where the majority of shock data was taken, and closer to the load wire at 2 mm. The probes were axially offset to avoid influencing the measurements, and oriented to measure azimuthal field. Traces from these experiments are shown in Figure 9. The data show that the probes recorded magnetic field in both radial positions. Initially, these signal are positive and cross zero and turn negative, consistent with a centroid of current passing the probe

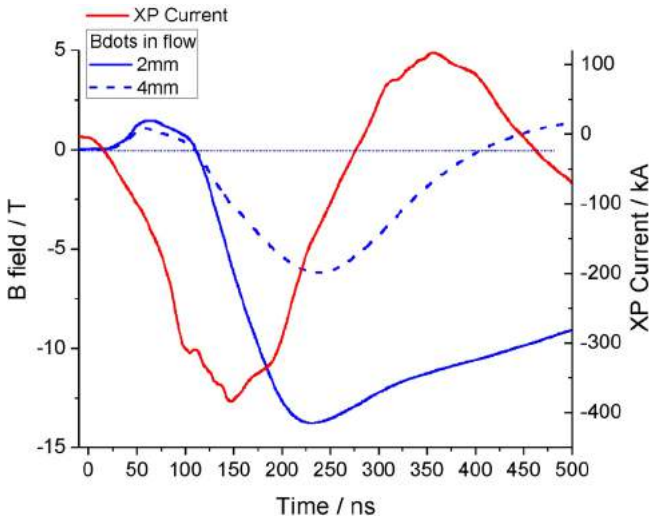


FIG. 9. Plots of integrated Bdot probe signals at 2 mm and 4 mm downstream of the load wire, along with the main experimental current drive.

locations.[34–36] At 2 mm the peak field is ~14 T and at 4 mm this is ~5 T. The bow-shocks are examined between 3 mm and 4 mm from the load wire, and we can infer the B-field of ~9 T at 3 mm. We can use these figures to estimate the plasma $\beta$ in the shock (ratio of plasma pressure to magnetic pressure) and hence determine if the B-field is likely to influence the structure here. Using the limits of the B-field and shock temperatures from the experiment, we can suggest a range of $\beta \sim 30$–130. The shock region is therefore dominated by the plasma pressure, and the B-field plays a very small role at this distance from the load wire.

## IV. COMPARISON TO SIMULATION

To investigate the bow-shock formation in detail, we have performed 2D simulations with the GORGON magneto-hydrodynamics code.[37] The experimental system is designed to be as "2D" as possible, in that the thickness of the plasma flow (out of the plane in Fig. 3, for example) is small compared to the other spatial scale lengths, and the obstruction protrudes for a significant distance either side of the flow, so that plasma cannot circumnavigate the obstruction. Additionally, the spatial resolution required for examine the shock formation is demanding, and a 3D simulation unfortunately becomes quickly prohibitive in terms of run time and resources. With these factors in mind, the use of a 2D simulation provides a reasonable approximation to the experiment for this system. The simulation is run on a Cartesian grid with a resolution of 6 $\mu$m over a region 10 mm × 8 mm. The inflow boundary (left hand boundary in the figures) uses a time dependent density profile generated from the rocket ablation model.[18] This uses the experimental current drive and therefore provides a good approximation to the experimental conditions. Figure 10 shows the formation of bow-shock for 2 targets in the flow, along with lineout of the electron and ion temperatures, and the electron density through the shock apex.

In general, the morphology is similar to that observed in the experiments and shows a high Mach number cone is

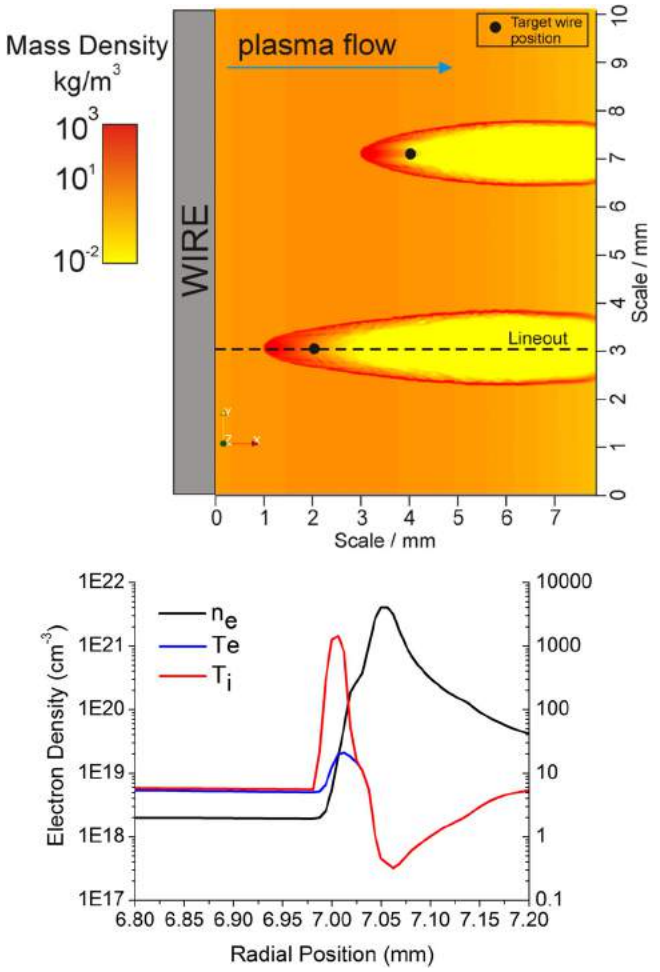


FIG. 10. 2D GORGON simulation of bow-shocks formed in ablating tungsten plasma flow: (top) mass density plot, and (bottom) lineouts at position indicated showing electron and ion temperatures and mass density as a function of position.

formed around each obstruction. As the flow impacts the target, the ion temperature increases rapidly to ~1 keV. Since the electron-ion equilibration time is short, the electron temperature rises to a peak of ~30 eV, before cooling through radiation loss due to the high downstream density. The radial extent over which the electron temperature is raised, i.e., where the plasma will emit radiation most strongly, is ~50 $\mu$m.

We can also use the simulation to investigate the effect of a magnetic field at the target convected with the flow. In Figure 11, we show plots of the same simulation set-up as is used to generate the plots in Figure 10. However, a fraction of the main drive current is caused to flow in the target wire: either 1%, 2%, or 5%. These plots are shown along with along with the self-emission experimental image on the same spatial scale. Increasing the B-field at the target has a distinct effect on the shock. Looking at the simulated self-emission images, the most highly emitting region at the shock apex increases in thickness by a factor of ~ 5 as the current increase by the same, since the magnetic pressure now influence the flow deceleration in addition to the hydrodynamics. The shape of the region close to the target wire as well as the entire Mach cone is significantly altered in the 5% plots. These features are not observed in the experiments

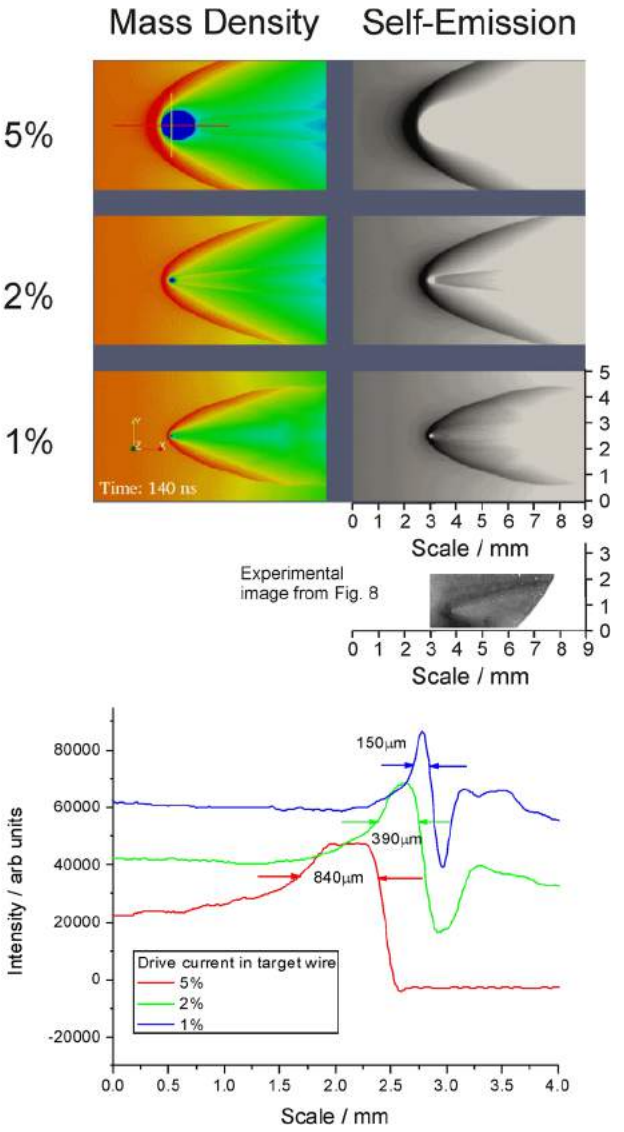


FIG. 11. 2D Gorgon simulations showing the effect of a fraction of the main drive current flowing in the target wire on the shock structure.

and indeed the highly emitting region is narrower than even the 1% case. This confirms the suggestion that magnetic pressure of any B-field in this region plays a negligible role and in line with our estimate of the plasma beta in the shock above.

## V. DISCUSSION

In this section, we discuss the shock structure in two parts. We primarily examine the shock structure observed at the shock apex, assuming this to be a planar, 1-dimensional shock along a line from the load wire to target. We also assess the implications for the remainder of the bow shock Mach cone.

The increase in temperature expected at the shock apex can be calculated from analytical theory as a function of the upstream Mach number, M, and the ratio of specific heats, $\gamma$

$$\frac{T'}{T} = \frac{\left[(\gamma-1)M^2+2\right]\left[2\gamma M^2-(\gamma+1)\right]}{(\gamma+1)^2 M^2}. \quad (3)$$

If we take a typical upstream Mach number of 6 and a pre-shock temperature of 15 eV, we can calculate the temperature increase for both adiabatic ($\gamma = 5/3$) and radiative ($\gamma = 4/3$) cases. For the adiabatic case, T'/T ~ 8.5 suggesting a post shock temperature of ~120 eV. For the radiative case, T'/T ~ 5.5, suggesting a post-shock temperature of ~65 eV. The latter of is clearly more in line estimates of 40–50 eV from Figure 7, indicating that the radiative values of $\gamma$ are more appropriate for this experiment.

Another perhaps a more appropriate approach is to use the upstream kinetic energy to estimate the effective value of $\gamma$. The upstream velocity is more fully characterized from previous studies in similar wire arrays (e.g., Ref. 20) and is likely more reliable in this sense. In the strong shock limit, Drake provides an expression for the downstream temperature as a function of the kinetic energy flow into the shock region[38]

$$k_B T_2 = \frac{A m_p}{(1+Z_2)} u_s^2 \frac{2(\gamma_2-1)}{(\gamma_2+1)^2}. \quad (4)$$

Using the value of $u_s = 100$ km/s and $Z_2 = 10$ as above, we can attempt to obtain a range of $\gamma$ value consistent with the data. From emission images in this work, we estimate $T_e \sim 40$–50 eV, as discussed above. We also note that the emission intensity at the shock region in the $h\nu > 160$ eV images (right image from Fig. 7) is similar to that of the plasma at the wire position. The most reliable experimental data for plasma temperature at this location is by Lebedev *et al.*[39] who took radially resolved gated XUV spectra for aluminum wire arrays. The estimate of the electron temperature close to the wire was ~40 eV. For a tungsten plasma, we might expect a lower temperature, since radiative cooling will be stronger, but this value serves as a useful guide. It is interesting to note that this is in line with the estimate from the present work.

For an upper bound on the temperature in the shock, we can examine Thomson scattering measurements by Harvey-Thompson *et al.*,[19] who discuss the collision of tungsten flows very similar to those in this work colliding at the axis of a cylindrical array. An accurate electron temperature determination was not possible, but the lack of ion acoustic resonances in the Thomson data suggested $Te < 100$ eV. Using Eq. (4), we can fit values of $\gamma$ consistent with these limits of the downstream temperature ($40\,\text{eV} < T_2 < 100\,\text{eV}$). This yields a range of $1.05 > \gamma > 1.15$ for the shock formation in the present study. The inverse sensitivity to the ionization state means that a lower Z value reduced the range of possible $\gamma$ values.

Behind the shock front, the ion temperature must equilibrate with the electron temperature which is dependent on the particle mean free paths (or equivalently collision frequencies) As noted in Figure 2, The ion-ion mean free path is small in relation to the system size, $\lambda_{\text{ion-ion}}/d_{\text{shock}} > 10$ for the times of interest. The electron-electron mean free path is shorter by a factor of the square root of the mass ratio. The electron-ion equilibration time is subsequently short, and the equilibration (or relaxation) length across the shock is $<1\,\mu$m. This is in general consistent with the narrow

emission region in Figure 9, which represents an upper limit as discussed above. The effects of electron heat conduction ahead of the shock are limited to spatial scales of order $\lambda_e \sim \chi_e/V_{flow}$, where $\chi_e$ is the electron thermal diffusivity $= (l_e\ v_{e,therm})/3$ ($\lambda_e =$ electron mean free path in the upstream flow, $v_{e,therm}$ is the thermal speed at 50 eV). Again this spatial scale is $< 1\ \mu$m and these mechanisms likely do not play a role outside the shock region itself.

The emission region observed ahead of the shock is interesting. From above, this is unlikely to be driven by particle transport ahead of the shock and is not the result of advected B-field. One possibility is the formation of a radiative precursor. Using estimates from Reighart *et al.*[7] and Drake,[40,41] we can determine if the shock is likely to be in the regime where radiative effects are important. Values calculated for the "radiative" parameter $R_r$ and the shock strength parameter are both in the range required and are similar to those determined in laser-driven shock experiments;[7] $R_r \sim 10^2$ (required $> 1$), $Q \sim 5 \times 10^5$ (require $> 5 \times 10^3$). Drake also gives analytical formula for the timescale for precursor formation along with the precursor length.[42] The timescale is $\sim$3 ns to form a precursor of $\sim 300\ \mu$m. The timescale is much shorter than the experiment timescale of $\sim$100 ns, and the experimental observation of the upstream emission region is $\sim 500\ \mu$m. However, the photon mean free path for energies consistent with the observed shock temperature is greater than the system size at $\sim$6 cm. It is unclear that a precursor in the diffusive or optically thin regime would form in these conditions. It may be possible, given the long timescales in this experiment, that a small fraction of radiation absorbed close to the shock has time to heat the upstream flow and influence the structure here. This is similar to a similar mechanism was suggested in gas-filled liner experiments by Burdiak *et al.*[43] who observed the formation of a radiative precursor in an optically thin upstream flow. The present work is not sufficiently conclusive to determine the nature of the upstream emission. It would be useful in future work to increase the upstream density, for example, by using the 1MA COBRA generator at Cornell University, which gives Rr and Q in the radiative regime, but a photon mean free path of $\sim 60\ \mu$m.

Away from the apex the upstream flow interacts with an oblique shock, where the transverse upstream velocity is some fraction of the full flow velocity, and the flow is redirected behind the shock. Effectively, the shock strength is reduced in these regions, with the velocity perpendicular to shock being the sine of the cone opening half angle. For example, in Figure 8, this is $\sim 20°$, so for 100 km/s the resulting velocity is 35 km/s, reducing the shock strength. Since the Mach cone angle is determined by the Mach number of the incoming flow, analysis of the shape here can be used to infer the time history of the flow. In the self-emission images, as well as interferometry image, the bow shock wings appear straight through the $\sim$4 mm region from the shock apex to the limit of the diagnostic viewing range. This suggests that the Mach number is relatively constant over this time period. The simulations show a greater range of radial position. At large radial separation from the load wire, several mm downstream of the target, the bow shock shape is curved. This suggest that at early time, the Mach number is significantly higher than around peak current, where most of the experimental analysis is carried out.

## V. CONCLUSIONS

We have demonstrated the formation of bow-shocks in tungsten plasma flows produced using an inverse wire array z-pinch, and that radiation loss plays an important role in such shocks. Measurements of the Mach cone opening angle as a function of distance from the load wire demonstrates Mach numbers $\sim$6. The Mach number may increase with increasing radius, as would be expected of a cooling flow. The shock emission width was determined through self-emission imaging to be $\leq 60\ \mu$m with peak temperatures $\sim$40–50 eV. This temperature jump is consistent with a radiative ratio of specific heats, $\gamma$, in the range 1.05–1.15 rather than the adiabatic case. The morphology, Mach cone formation and shock emission width are consistent with detailed 2D simulations. Bdot probe measurements in the plasma flow along examination of the effect of advected B-field through the simulations, suggest that the shock has $\beta \sim 100$. The shock formation is hydrodynamic, with magnetic field playing no role in the shock structure for these experiments.

The experimental system in this work may have advantages over other methods used to produce shocks in which radiation loss is important. The shock is stationary in the lab frame, which allows detailed work with high spatial resolution to study evolution. Additionally, the relative invariance of the flow velocity with drive current means that experiments can be carried out with moderate facilities, although higher current will allow more effective application of radiography techniques to allow direct quantification of the density jump, as well as allowing a clearer examination of the effects of optical depth close to the shock. Another obvious extension is to allow current to flow in the target wire and drive a magnetic field here, allowing detailed examination investigation of magnetized bow-shock. This work is presently underway and will be reported in a future article.

## ACKNOWLEDGMENTS

This work was funded through Department of Energy Contract No. DE-SC0006958, and work at Cornell University was supported under the NNSA Stockpile Stewardship Academic Alliance program through DOE Cooperative Agreement No. DE-NA0001836. The authors gratefully acknowledge the help of Todd Blanchard and Harry Wilhelm during the experiments.

[1]B. Reipurth and J. Bally, Annu. Rev. Astron. Astrophys. **39**, 403 (2001).
[2]P. Hartigan, A. Frank, J. M. Foster, B. H. Wilde, M. Douglas, P. A. Rosen, R. F. Coker, B. E. Blue, and J. F. Hansen, Ap. J. **736**, 29 (2011).
[3]W. J. M. Rankine, Philos. Trans. R. Soc. London **160**, 277 (1870).
[4]H. Hugoniot, J. Polytech. **57**, 3–97 (1887); **58**, 1 (1889).
[5]*Physics of Shock Waves and High Temperature Hydrodynamic Phenomena*, edited by Ya. B. Zel'dovich and Yu. P. Raizer, 2nd ed. (Dover Publications Inc, 2002).
[6]C. E. Needham, *Blast Waves: Shock Wave and High Pressure Phenomena* (Springer, 2010), pp. 9–15.
[7]A. B. Reighart, R. P. Drake, K. K. Dannenberg, D. J. Kremer, M. Grosskopf, E. C. Harding, D. R. Leibrandt, S. G. Glendinning, T. S. Perry,

B. A. Remington, J. Greenough, J. Knauer, T. Boehly, S. Bouquet, L. Boireau, M. Koenig, and T. Vinci, Phys. Plasmas **13**, 082901 (2006).
[8]J. C. Bozier, G. Thiell, J. P. Le Breton, S. Azra, M. Decroisette, and D. Schirmann, Phys. Rev. Lett. **57**, 1304 (1986).
[9]J. Grun, J. Stamper, C. Manka, J. Resnick, R. Burris, J. Crawford, and B. H. Ripin, Phys. Rev. Lett. **66**, 2738 (1991).
[10]S. Bouquet, C. Stéhlé, M. Koenig, J.-P. Chièze, A. Benuzzi-Mounaix, D. Batani, S. Leygnac, X. Fleury, H. Merdji, C. Michaut, F. Thais, N. Grandjouan, T. Hall, E. Henry, V. Malka, and J.-P. J. Lafon, Phys. Rev. Lett. **92**, 225001 (2004).
[11]M. Koenig, A. Benuzzi-Mounaix, N. Grandjouan, V. Malka, S. Bouquet, X. Fleury, B. Marchet, Ch. Stehle, S. Leygnac, C. Michaut, J. P. Chieze, D. Batani, E. Henry, and T. Hall, *Shock Compression of Condensed Matter-2001* (2001), p. 1367.
[12]M. Koenig, T. Vinci, A. Benuzzi-Mounaix, S. Lepape, N. Ozaki, S. Bouquet, L. Boireau, S. Leygnac, C. Michaut, C. Stehle, J.-P. Chieze, D. Batanis, T. Hall, K. Tanaka, and M. Yoshida, Astrophys. Space Sci. **298**, 69 (2005).
[13]T. Vinci, Phys. Plasmas **13**, 010702 (2006).
[14]M. Hohenberger, D. R. Symes, J. Lazarus, H. W. Doyle, R. E. Carley, A. S. Moore, E. T. Gumbrell, M. M. Notley, R. J. Clarke, M. Dunne, and R. A. Smith, Phys. Rev. Lett. **105**, 205003 (2010).
[15]D. J. Ampleford, C. A. Jennings, G. N. Hall, S. V. Lebedev, S. N. Bland, S. C. Bott, F. Suzuki-Vidal, J. B. A. Palmer, J. P. Chittenden, M. E. Cuneo, A. Frank, and E. G. Blackman, Phys. Plasmas **17**, 056315 (2010).
[16]J. L. Peebles, S. C. Bott, K. Gunasekera, J. Kim, L. Harpster, B. Evans, D. Gomez, O. Paran, C. Peterson, and F. N. Beg, IEEE Trans. Plasma Sci. **39**, 2422 (2011).
[17]A. Harvey-Thompson, S. V. Lebedev, S. N. Bland, J. P. Chittenden, G. N. Hall, A. Marocchino, F. Suzuki-Vidal, S. C. Bott, J. B. A. Palmer, and C. Ning, Phys. Plasmas **16**, 022701 (2009).
[18]S. V. Lebedev, F. N. Beg, S. N. Bland, J. P. Chittenden, A. E. Dangor, M. G. Haines, K. H. Kwek, S. A. Pikuz, and T. A. Shelkovenko, Phys. Plasmas **8**, 3734 (2001).
[19]A. J. Harvey-Thompson, S. V. Lebedev, S. Patankar, S. N. Bland, G. Burdiak, J. P. Chittenden, A. Colaitis, P. De Grouchy, G. N. Hall, E. Khoory, M. Hohenberger, L. Pickworth, F. Suzuki-Vidal, R. A. Smith, J. Skidmore, L. Suttle, and G. F. Swadling, Phys. Plasmas **19**, 056303 (2012).
[20]A. J. Harvey-Thompson, S. V. Lebedev, S. Patankar, S. N. Bland, G. Burdiak, J. P. Chittenden, A. Colaitis, P. De Grouchy, H. W. Doyle, G. N. Hall, E. Khoory, M. Hohenberger, L. Pickworth, F. Suzuki-Vidal, R. A. Smith, J. Skidmore, L. Suttle, and G. F. Swadling, Phys. Rev. Lett. **108**, 145002 (2012).
[21]S. V. Lebedev, L. Suttle, G. F. Swadling, M. Bennett, S. N. Bland, G. C. Burdiak, D. Burgess, J. P. Chittenden, A. Ciardi, A. Clemens, P. de Grouchy, G. N. Hall, J. D. Hare, N. Kalmoni, N. Niasse, S. Patankar, L. Sheng, R. A. Smith, F. Suzuki-Vidal, J. Yuan, A. Frank, E. G. Blackman, and R. P. Drake, Phys. Plasmas **21**, 056305 (2014).
[22]D. H. Kalantar, Ph.D. dissertation, Cornell University, May 1993.
[23]F. F. Chen, *Introduction to Plasma Physics and Controlled Fusion: Vol 1*, 2nd ed. (Springer, 1983), p. 352.
[24]M. Sherlock, J. P. Chittenden, S. V. Lebedev, and M. G. Haines, Phys. Plasmas **11**, 1609 (2004).
[25]D. Salzman, *Atomic Physics in Hot Plasmas* (Oxford University Press, 1998), p. 23.
[26]S. C. Bott, D. M. Haas, Y. Eshaq, U. Ueda, S. V. Lebedev, J. P. Chittenden, J. B. A. Palmer, S. N. Bland, G. N. Hall, D. J. Ampleford, and F. N. Beg, IEEE Trans. Plasma. Sci. **36**, 2759 (2008).
[27]S. C. Bott, G. Collins IV, K. Gunasekera, D. Mariscal, F. N. Beg, D. M. Haas, F. Veloso, I. C. Blesener, A. D. Cahill, C. L. Hoyt, B. R. Kusse, and D. A. Hammer, Rev. Sci. Intrum. **83**, 083507 (2012).
[28]IDEA, V1.7, Graz University of Technology, Austria (http://optics.tu-graz.ac.at).
[29]M. Hipp, J. Woisetschleager, P. Reiterer, and T. Neger, Measurement **36**, 53 (2004).
[30]*Principles of Plasma Diagnostics*, edited by I. H. Hutchinson, 2nd ed. (Cambridge University Press, 2002).
[31]S. C. Bott, S. V. Lebedev, F. N. Beg, S. N. Bland, J. P. Chittenden, A. Ciardi, M. G. Haines, D. J. Ampleford, C. Jennings, J. Rapley, J. Palmer, and M. Sherlock, Phys. Rev. E **74**, 046403 (2006).
[32]S. C. Bott, D. M. Haas, Y. Eshaq, U. Ueda, F. N. Beg, D. A. Hammer, B. Kusse, J. Greenly, T. A. Shelkovenko, S. A. Pikuz, I. C. Blesener, R. D. McBride, J. D. Douglass, K. Bell, P. Knapp, J. P. Chittenden, S. V. Lebedev, S. N. Bland, G. N. Hall, F. A. Suzuki Vidal, A. Marocchino, A. Harvey-Thomson, M. G. Haines, J. B. A. Palmer, A. Esaulov, and D. J. Ampleford, Phys Plasmas **16**, 072701 (2009).
[33]S. V. Lebedev, R. Aliaga-Rossel, S. N. Bland, J. P. Chittenden, A. E. Dangor, M. G. Haines, and I. H. Mitchell, Phys. Plasmas **6**, 2016 (1999).
[34]J. Greenly, M. Martin, I. Blesener, D. Chalenksi, P. Knapp, and R. McBride, AIP Conf. Proc. **1088**, 53 (2009).
[35]V. V. Aleksandrov, G. S. Volkov, E. V. Grabovski, V. I. Zaitsev, G. G. Zukakishvili, S. F. Medovschikov, K. N. Mitrofanov, S. L. Nedoseev, G. M. Oleinik, I. Y. Porofeev, A. A. Samokhin, P. V. Sasorov, V. P. Smirnov, I. N. Frolov, and M. V. Fedulov, AIP Conf. Proc. **808**, 3 (2006).
[36]M. R. Martin, C. E. Seyler, and J. B. Greenly, Phys. Plasmas **17**, 052706 (2010).
[37]J. P. Chittenden, S. V. Lebedev, C. A. Jennings, S. N. Bland, and A. Ciardi, Plasma Phys. Controlled Fusion **46**, B457–B476 (2004).
[38]R. P. Drake, *High-Energy-Density Physics: Fundamentals, Inertial Fusion, and Experimental Astrophysics (Shock Wave and High Pressure Phenomena)* (Springer Press, 2006), pp. 115–116.
[39]S. V. Lebedev, F. N. Beg, S. N. Bland, J. P. Chittenden, A. E. Dangor, M. G. Haines, S. A. Pikuz, and T. A. Shelkovenko, Laser Particle Beams **19**, 355–376 (2001).
[40]R. P. Drake, Phys. Plasmas **14**, 043301 (2007).
[41]R. P. Drake, IEEE Trans. Plasma Sci. **35**, 171 (2007).
[42]R. P. Drake, *High-Energy-Density Physics: Fundamentals, Inertial Fusion, and Experimental Astrophysics (Shock Wave and High Pressure Phenomena)* (Springer Press, 2006), pp. 309–313.
[43]G. C. Burdiak, S. V. Lebedev, R. P. Drake, A. J. Harvey-Thompson, G. F. Swadling, F. Suzuki-Vidal, J. Skidmore, L. Suttle, E. Khoory, L. Pickworth, P. de Grouchy, G. N. Hall, S. N. Bland, M. Weinwurm, and J. P. Chittenden, High Energy Density Phys. **9**, 52–62 (2013).